

# Analysis and Reduction of Current and Voltage Ripple in DC Link for Three-Level NPC Inverter-Fed Dual Three-Phase Motor Drives

Minrui Gu, *Student Member, IEEE*, Zheng Wang<sup>✉</sup>, *Senior Member, IEEE*, and Obrad Dordevic<sup>✉</sup>, *Member, IEEE*

**Abstract**—In this article, switching strategies for dc-link current and voltage ripple reduction have been studied. The considered topology is a neutral-point clamped three-level (NPC-3L) inverter feeding a dual three-phase permanent-magnet synchronous motor (PMSM). The mechanisms of dc-link current and voltage ripple generation in an NPC-3L inverter-fed PMSM drive are analyzed in detail. Then, a two-step collaborative switching strategy is proposed, where the optimum switching sequences, including opposite small vectors, are applied in the two inverters collaboratively. Furthermore, the switching vectors of two inverters are rearranged in the sequence of their corresponding dc-link capacitor currents so that the overlapping of their peaks is avoided. Consequently, both the voltage ripple and current ripple in the dc-link capacitors are mitigated with the proposed two-step collaborative switching strategy. For the midpoint voltage of the NPC-3L inverter, the amplitude of fluctuation is reduced under low modulation index operation, while the high-frequency harmonic components are mitigated under high modulation index operation. The experimental results are given to verify the validity of the theoretical analysis and the proposed switching strategy.

**Index Terms**—Current and voltage ripple, dc-link capacitor, dual three-phase permanent-magnet synchronous motor (PMSM) drive, neutral-point clamped three-level (NPC-3L) inverter, switching strategy.

## I. INTRODUCTION

RECENTLY, with the increasing demands for power capacity and reliability, multiphase motor drives have received wide attention in industrial applications. When compared to three-phase drives, multiphase drives offer the merits of lower torque pulsation, lower current stress for switching devices, higher fault-tolerant capability, and additional degrees

of control freedom [1], [2], [3]. A dual three-phase drive is an attractive solution with a capability to eliminate sixth-order torque harmonic pulsation and has been commercialized in various fields including wind energy generation [4]. On the other hand, the diode-clamped neutral-point clamped three-level (NPC-3L) converter is popular for medium-voltage high-power drives (typically 3–6.6 kV) due to the superiority of lower voltage stress across the switching devices, lower output current and voltage harmonic distortion, and lower electromagnetic interference [5], [6], [7]. Therefore, it is a popular choice for high-power medium-voltage drives. By combining these technologies, the performance can be further improved in multilevel multiphase drives [8], [9].

The reliability of drives involves evaluation of switching device modules, electric machines, current and voltage sensors, speed sensors, dc-link capacitors, and other components in the system [10], [11]. It was found in [11] that capacitor failure accounts for 30% of all failures in a power converter. Therefore, the dc-link capacitor lifetime is one of the main factors concerning the reliability of motor drives. Usually, the electrolytic capacitors are used in the dc link due to large capacitance, relatively low cost, and small sizes. The expected lifetime of the electrolytic capacitor is extremely sensitive to the rise of operating temperature, which is caused by the ripple current in the equivalent series resistor [12], [13], [14].

Consequently, research works have been published on capacitor current ripple reduction, for the extension of capacitor lifetime and the enhancement of system reliability [15], [16], [17], [18], [19]. An optimized switching strategy for a three-level T-type NPC (T-NPC) inverter was proposed in [15], where the two opposite active voltage vectors, rather than zero-state vectors, are utilized to synthesize the reference voltage vector. Thus, the large current ripple generated by the zero-state vector is avoided. The optimized switching strategy was further experimentally verified for a three-level photovoltaic inverter in [16]. However, current ripple reduction at low modulation indexes was not so significant. In [17], a reduction method of current ripple was proposed for active neutral-point clamped inverters for the full modulation-index range. In the low modulation index region, only the medium-voltage vectors are used for the synthesis of the reference voltage vector. In the high modulation index region, hybrid modulation (including medium-vector modulation and the modulation of [15] and [16]) is utilized. However, the impact

Manuscript received 29 March 2022; revised 12 August 2022 and 8 October 2022; accepted 11 November 2022. Date of publication 23 November 2022; date of current version 14 February 2023. This work was supported in part by the Aeronautical Science Foundation of China under Grant 20200019069001 and in part by the National Natural Science Foundation of China under Grant 52077034. Recommended for publication by Associate Editor M. Hagiwara. (Corresponding author: Zheng Wang.)

Minrui Gu and Zheng Wang are with the School of Electrical Engineering, Southeast University, Nanjing 210096, China (e-mail: 230228726@seu.edu.cn; zwang@eee.hku.hk).

Obrad Dordevic is with the Department of Electronics and Electrical Engineering, Liverpool John Moores University, Liverpool L3 3AF, U.K. (e-mail: o.dordevic@ljmu.ac.uk).

Color versions of one or more figures in this article are available at <https://doi.org/10.1109/TPEL.2022.3224125>.

Digital Object Identifier 10.1109/TPEL.2022.3224125

of the power factor on the current ripple has not been considered in the above methods [18]. In [19], a generalized switching modulation method using the carrier shift method was proposed for a dc–dc–ac system to reduce the dc-link current ripple.

It should be noted that all the aforementioned analysis and control methods for the dc-link current ripple reduction are limited to three-phase drive systems, and related research on multiphase drive systems is very scarce. In [20], a collaborative method was proposed to reduce the current ripple of a dual three-phase permanent-magnet synchronous motor (PMSM) drive by sorting the voltage vectors in a sequence corresponding to their dc-link currents. Thus, more dimensions of control freedom offered by multiphase drive systems have been utilized. However, a two-level inverter topology was used in [20]. For multilevel multiphase drives, the study of collaborative switching strategy for reducing dc-link current ripples is still absent.

Meanwhile, special attention is also required for the dc-link voltage ripple as it determines the sizing of the dc-link capacitors. In [21], the dc-link voltage ripple was analyzed for three-phase inverters under unbalanced load. In [22] and [23], the voltage ripple using space vector modulation (SVM) was compared to those using sinusoidal PWM and discontinuous PWM (DPWM). In [24], [25], and [26], studies have been presented for the dc-link voltage ripple in multiphase inverters. In [24], voltage ripple was analyzed for the seven-phase inverter. In [25], design guidelines were provided for the selection of dc-link capacitors in multiphase inverters based on the peak-to-peak value of the dc-link voltage ripple. However, only two-level inverters are discussed in these studies. In [26], mitigation of the dc-link capacitor voltage ripple was studied for T-NPC inverter-fed six-phase motor drive, where two sets of three-phase windings are wound in two separate halves of the stator. The output current of one three-phase T-NPC inverter is out of phase with that of the second three-phase T-NPC inverter, resulting in naturally balanced dc-link capacitor voltages. However, the dc-link voltage ripple caused by the switching actions was not studied. Moreover, output currents of each inverter are opposite to each other in [26], which may limit the performance if applied to other types of dual three-phase drives with different shift angles.

Therefore, to the best of the authors' knowledge, related studies of the dc-link voltage and current ripple for multilevel multiphase drives are still rare, in particular, for systems with wide modulation index and power factor range. This article tackles this problem by proposing a two-step collaborative switching strategy (TSCSS). With the proposed strategy, the dc-link capacitor current and voltage ripple can be reduced simultaneously.

The rest of this article is organized as follows. Configuration and control of the analyzed NPC-3L inverter-fed dual three-phase PMSM drive are presented in Section II. Then, the mechanisms of capacitor current and voltage ripple formation, with the synchronous switching pattern, are analyzed in Section III. In Section IV, a TSCSS is proposed. Its performance is investigated in Section V for different modulation indexes and power factors. In Section VI, experimental results are presented to verify the effectiveness of the proposed switching strategy. Finally, Section VII concludes this article.

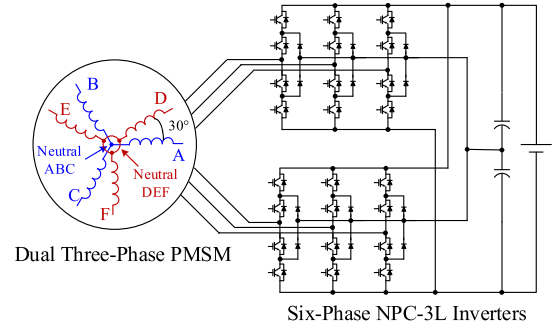


Fig. 1. Configuration of the NPC-3L inverter-fed dual three-phase PMSM drive.

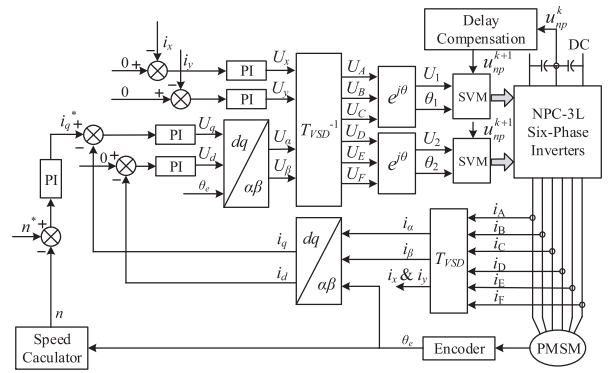


Fig. 2. Diagram of the basic control scheme.

## II. CONFIGURATION AND CONTROL SCHEME

Fig. 1 shows configuration of the analyzed NPC-3L inverter-fed dual three-phase PMSM drive. Note that although a diode-clamped NPC topology is used in this article, the same derivations and results would also apply to the T-NPC topology because the modulation complexity of these two topologies is equivalent [27]. With the increase of semiconductor voltage ratings, the T-NPC converter is becoming a promising competitor to diode-clamped NPC converter, for high-power medium-voltage drives, due to its merits such as higher efficiency and lower device number [28]. The three-phase winding sets of the machine are shifted by  $30^\circ$ , and the neutral points of the two winding sets are isolated. The decoupled mathematical model of the dual three-phase PMSM can be obtained using vector space decomposition (VSD) as in [29].

Fig. 2 shows the block diagram of the control scheme. The PI controller is used to regulate the speed of the machine. After the application of VSD transformation, a field-oriented control scheme is utilized to regulate the current components in the  $\alpha$ - $\beta$  subspace. Reference voltages  $U_\alpha$  and  $U_\beta$  in the  $\alpha$ - $\beta$  subspace and  $U_x$  and  $U_y$  in the  $x$ - $y$  subspace are generated by the corresponding four closed-loop current controllers. As shown in Fig. 2, reference voltages  $U_A$ ,  $U_B$ ,  $U_C$ ,  $U_D$ ,  $U_E$ , and  $U_F$  in the natural reference frame are obtained from  $U_\alpha$ ,  $U_\beta$ ,  $U_x$ , and  $U_y$ , using the inverse VSD transformation matrix  $T_{VSD}^{-1}$ . Then, three-phase SVM is conducted separately for each of the two sets using the algorithm of [30]. The delay compensation module is utilized to compensate for the digital controller delay effects.

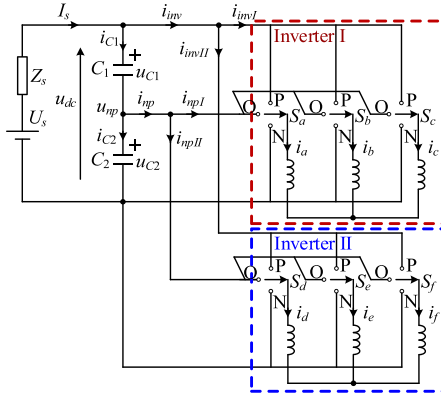


Fig. 3. Equivalent circuit of the three-phase drive.

### III. ANALYSIS OF CAPACITOR CURRENTS AND VOLTAGES WITH SYNCHRONOUS SWITCHING STRATEGY (SSS)

#### A. Synchronous SVM Modulation

Fig. 3 shows the equivalent circuit of the dual three-phase motor drive, where  $Z_s$  is the equivalent dc-source impedance, and  $C_1$  and  $C_2$  are the dc-link capacitors. Capacitor currents are denoted by  $i_{C1}$  and  $i_{C2}$ , respectively, whereas  $i_a, i_b,$  and  $i_c$  and  $i_d, i_e,$  and  $i_f$  are the stator set 1 and set 2 currents, respectively. The inverter input and the neutral point current are denoted by  $i_{inv}$  and  $i_{np}$ , respectively. Furthermore,  $i_{invI}$  denotes the input current of inverter I, whereas  $i_{invII}$  denotes the input current of inverter II. Similarly,  $i_{npI}$  and  $i_{npII}$  denote the neutral point currents generated by inverters I and II, respectively. Therefore,  $i_{inv} = i_{invI} + i_{invII}$  and  $i_{np} = i_{npI} + i_{npII}$ . The dc-source voltage and current are denoted by  $U_s$  and  $I_s$ , respectively.

Generally, the current ripple at the switching frequency can be assumed to only pass through the branch with the capacitors [25]. Based on the power balance principle, and the assumption that the power switches are ideal, one gets

$$I_s = 3mI_0 \cos \varphi \quad (1)$$

where  $I_0$  represents the amplitude of the stator currents,  $\varphi$  is the power factor angle, and  $m$  is the modulation index ( $m = V_0/u_{dc}$ , where  $V_0$  is the amplitude of the output phase voltage and  $u_{dc}$  is the dc-link voltage). Each leg of the NPC-3L inverter can be regarded as a single-pole three-throw switch, which generates three voltage levels, i.e., P, O, and N level. For convenience, the switch function is defined as

$$S_x = \begin{cases} 1 & \text{output P level} \\ 0 & \text{output O level} \\ -1 & \text{output N level} \end{cases} \quad x \in \{a, b, c, d, e, f\} \quad (2)$$

Consequently,  $i_{inv}$  and  $i_{np}$  can be expressed as

$$i_{inv} = \sum_x \frac{1}{2} (S_x^2 + S_x) i_x, \quad x \in \{a, b, c, d, e, f\} \quad (3)$$

$$i_{np} = \sum_x (1 - S_x^2) i_x, \quad x \in \{a, b, c, d, e, f\} \quad (4)$$

Capacitor currents  $i_{C1}$  and  $i_{C2}$  can be expressed as

$$i_{C1} = I_s - i_{inv} = I_s - i_{C1-s} \quad (5)$$

$$i_{C2} = i_{C1} - i_{np} = I_s - (i_{inv} + i_{np}) = I_s - i_{C2-s} \quad (6)$$

where  $i_{C1-s}$  and  $i_{C2-s}$  denote the current components in  $i_{C1}$  and  $i_{C2}$ , respectively, determined by the inverter switching actions. Both  $i_{C1-s}$  and  $i_{C2-s}$  contain current components influenced by both inverters, as

$$i_{C1-s} = i_{C1-sI} + i_{C1-sII} = i_{invI} + i_{invII} \quad (7)$$

$$i_{C2-s} = i_{C2-sI} + i_{C2-sII} = (i_{invI} + i_{npI}) + (i_{invII} + i_{npII}) \quad (8)$$

where  $i_{C1-sI}$  and  $i_{C2-sI}$  denote  $i_{C1-s}$  and  $i_{C2-s}$  generated by inverter I, respectively, whereas  $i_{C1-sII}$  and  $i_{C2-sII}$  denote  $i_{C1-s}$  and  $i_{C2-s}$  generated by inverter II, respectively. Therefore,  $i_{C1-sI} = i_{invI}$ ,  $i_{C2-sI} = i_{invI} + i_{npI}$ ,  $i_{C1-sII} = i_{invII}$ , and  $i_{C2-sII} = i_{invII} + i_{npII}$ . Furthermore, the dc-link voltage  $u_{dc}$  can be expressed as

$$\begin{aligned} u_{dc} &= u_{C1} + u_{C2} = U_{dc\_ave} + \frac{1}{C} \int_{t_0}^{t_0+T_s} (i_{C1} + i_{C2}) dt \\ &= U_{dc\_ave} + \frac{1}{C} \int_{t_0}^{t_0+T_s} [2I_s - (2i_{inv} + i_{np})] dt. \end{aligned} \quad (9)$$

While setting the reference node as half of the dc-link, the actual midpoint voltage  $u_{np}$  can be given as

$$u_{np} = \frac{u_{C2} - u_{C1}}{2}. \quad (10)$$

Above,  $T_s$  denotes the switching period and  $t_0$  is the initial instant of the switching period.  $u_{C1}$  and  $u_{C2}$  are the voltages of the capacitors  $C_1$  and  $C_2$ , respectively.  $U_{dc\_ave}$  is the average dc-link voltage, which also equals the initial value of  $u_{dc}$  at instant  $t_0$ .  $C$  is the capacitance value of  $C_1$  and  $C_2$ . It is noted that the switching sequence applied from instant  $(k+1)T_s$  to instant  $(k+2)T_s$  is calculated based on the sampled information at instant  $kT_s$ . Therefore, there exists a delay effect in digital implementation, and crucial information at the future instant  $(k+1)T_s$  requires to be predicted. The predicted midpoint voltage can be calculated as

$$u_{np}^{k+1} = u_{np}^k - \frac{1}{2C} \sum_i^{\text{seg}^k} i_{np-i}^k t_i^k \quad (11)$$

where  $u_{np}^k$  is the value at instant  $kT_s$ , and  $u_{np}^{k+1}$  is the predicted value at instant  $(k+1)T_s$ .  $i_{np-i}^k$  is  $i_{np}$  generated in the  $i$ th segment by the applied switching state,  $t_i^k$  is the dwell time of the  $i$ th segment from instant  $kT_s$  to  $(k+1)T_s$ , and  $\text{seg}^k$  is the total number of segments from instant  $kT_s$  to  $(k+1)T_s$ . It can be observed from (3)–(11) that current and voltage expressions are directly related to the applied switching states. Therefore, the switching sequence of the modulation scheme can be optimized to improve the performance of the dc-link current and voltage.

Fig. 4(a) shows space vector diagram for the three-phase NPC-3L inverter. There are 27 vectors in total, which include six redundant small vectors and three zero vectors. The plane is separated into six sectors S1–S6, where each sector consists of four triangular regions. In the SVM scheme, the nearest three

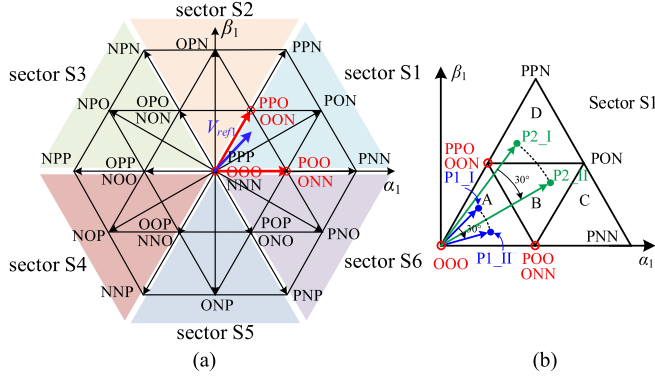


Fig. 4. Space vector diagram of three-phase NPC-3L inverter. (a) Diagram of the whole inverter. (b) Diagram of sector S1.

vectors are selected to synthesize the reference voltage vector. To reduce the switching actions while keeping good harmonic performance, the switching sequence is arranged as in [31], which is a kind of DPWM strategy [32]. The lower voltage levels are placed at the beginning and at the end of a switching period, while the higher voltage levels are placed in the middle, for each leg of the inverter. For instance, if the reference voltage vector is located in region A of sector S1, as shown in Fig. 4(b), the vectors PPO, OON, POO, ONN, and OOO are selected. Then, the switching sequence with positive small vectors is OOO-PPO-PPO-POO-OOO, whereas the switching sequence with negative small vectors is ONN-ONN-OOO-ONN-ONN. The choice of positive or negative small vectors is determined by control of the midpoint voltage. When the midpoint voltage is larger than the desired value, the negative small vectors are selected to reduce the midpoint voltage, and vice versa. Conventionally, both inverters would follow the same DPWM rules, and this category of switching sequence arrangement is called synchronous modulation, in this article.

### B. Analysis of Current and Voltage Ripples

As can be seen from Fig. 4(a), the space vector diagram of the three-level three-phase inverter has a radial symmetry with the base region spanning  $60^\circ$ . Assuming a symmetric load, the current and voltage ripple pattern will follow the same symmetry, and therefore, only one sector (1/6 of the fundamental period) is analyzed. For further analysis, sector S1 has been chosen with few typical operating points, as indicated in Fig. 4(b). Considering only the fundamental components and neglecting the switching harmonics, the output voltages and currents can be expressed as

$$u_i = \begin{cases} V_0 \cos(\omega t - 2\pi/3 \cdot (i-1)), & i \in \{1, 2, 3\} \\ V_0 \cos(\omega t - 2\pi/3 \cdot (i-4) - \pi/6), & i \in \{4, 5, 6\} \end{cases} \quad (12)$$

$$i_i = \begin{cases} I_0 \cos(\omega t - 2\pi/3 \cdot (i-1) + \varphi), & i \in \{1, 2, 3\} \\ I_0 \cos(\omega t - 2\pi/3 \cdot (i-4) + \varphi - \pi/6), & i \in \{4, 5, 6\} \end{cases} \quad (13)$$

where  $u_i$  and  $i_i$  are the voltage and current in phase  $i$ , respectively,  $V_0$  and  $I_0$  are the corresponding amplitudes, and  $\omega$  is the angular

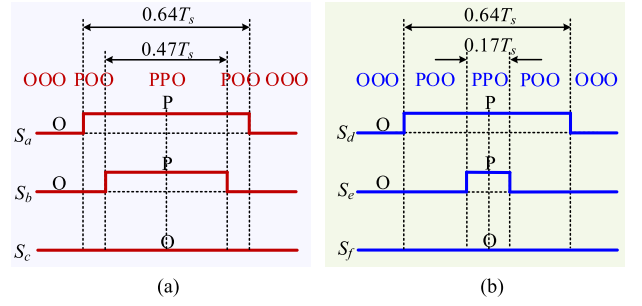


Fig. 5. Switching patterns of the two inverters at points P1\_I and P1\_II with the sequence with positive small vectors. (a) Inverter I. (b) Inverter II.

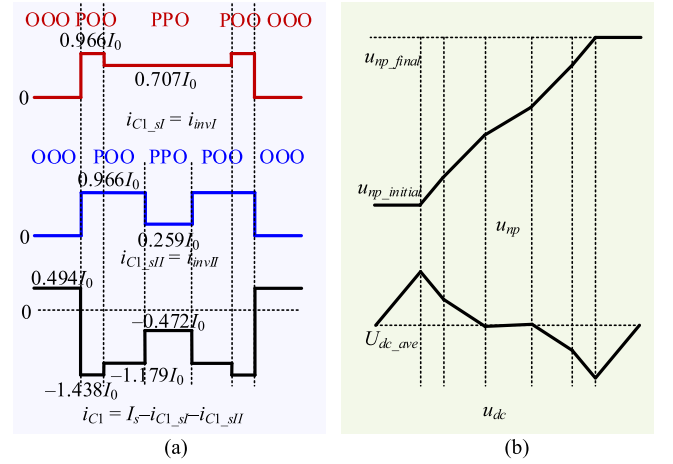


Fig. 6. Current and voltage waveforms during a single switching period with the sequence with positive small vectors at points P1\_I and P1\_II. (a) Current waveforms of capacitor  $C_1$ . (b) Waveforms of midpoint and DC-link voltage.

frequency. The values of  $i$  equal to 1, 2, and 3 correspond to phases A, B, and C (the first three-phase set), and similarly 4, 5, and 6 are used for D, E, and F (the second three-phase set). The power factor angle  $\varphi$  is given as  $-\pi/6$  considering the normal operation of PMSM.

It is worth noting that the effect of parasitic inductance is ignored in the following dc-link current and voltage ripple analysis [20], [25]. In reality, the actual capacitor current would not change in a step manner, as will be demonstrated later on in Section VI. However, the used approach is accurate enough to indicate where the ripple has its peaks, and based on that, a new switching strategy is developed in this article, which effectively reduces the ripple.

As shown in Fig. 4(b), the first selected operating point is P1, where the reference vector for inverter I is located at point P1\_I and at point P1\_II for inverter II. In this example, the modulation index is  $m = 0.19$ , and the phase angles of P1\_I and P1\_II are  $\pi/4$  and  $\pi/12$ , respectively. Using (13) one gets  $i_a = 0.966I_0$ ,  $i_b = -0.259I_0$ ,  $i_c = -0.707I_0$ ,  $i_d = 0.966I_0$ ,  $i_e = -0.707I_0$ , and  $i_f = -0.259I_0$ . Also, based on (1), the dc-source current  $I_s$  is equal to  $0.494I_0$ . Fig. 5 shows the switching patterns using the positive small vectors, applied when the midpoint voltage  $u_{np}^{k+1}$  is below the desired value. As shown in Fig. 5, the dwell times for vectors OOO, POO, and PPO are  $0.36T_s$ ,  $0.17T_s$ , and  $0.47T_s$

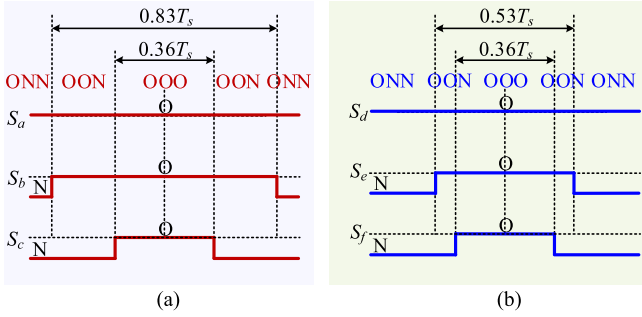


Fig. 7. Switching patterns of the two inverters at points P1\_I and P1\_II with the sequence with negative small vectors. (a) Inverter I. (b) Inverter II.

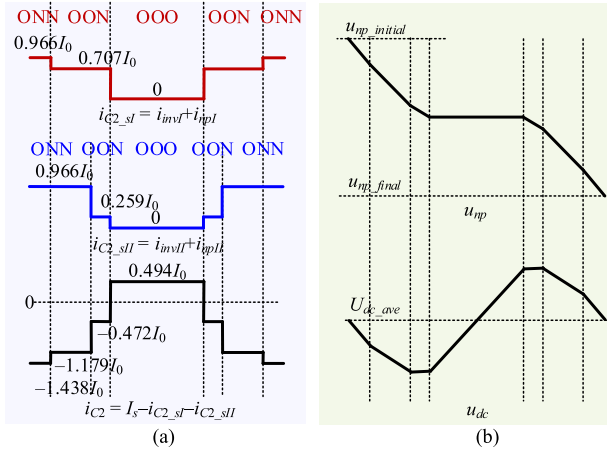


Fig. 8. Current and voltage waveforms during a single switching period with the sequence with negative small vectors at points P1\_I and P1\_II. (a) Current waveforms of capacitor C<sub>2</sub>. (b) Waveforms of midpoint and DC-link voltage.

in inverter I, respectively. On the other hand, the dwell times for vectors OOO, POO, and PPO in inverter II are  $0.36T_s$ ,  $0.47T_s$ , and  $0.17T_s$ , respectively.

With the switching patterns shown in Fig. 5, the waveforms of  $i_{C1}$  and  $u_{dc}$  are analyzed, as shown in Fig. 6. Based on (3), (4), and (6),  $i_{C2}$  equals  $I_s$  when positive small vectors or zero vectors are used. Therefore, the waveform of  $i_{C2}$  is not discussed in Fig. 6. As shown in Fig. 6(a),  $i_{C1-sI}$  equals 0,  $i_a$  ( $0.966I_0$ ), and  $i_a + i_b = -i_c$  ( $0.707I_0$ ), when the vectors OOO, POO, and PPO are used in inverter I, respectively. Similarly,  $i_{C1-sII}$  equals 0,  $i_d$  ( $0.966I_0$ ), and  $i_d + i_e = -i_f$  ( $0.259I_0$ ), when vectors OOO, POO, and PPO are used in inverter II, respectively. It is observed that maximum as well as minimum current levels of  $i_{C1-sI}$  and  $i_{C1-sII}$  overlap each other. Consequently, large current ripple can be observed in the waveform of  $i_{C1}$ .

Fig. 6(b) shows the waveforms of the midpoint voltage  $u_{np}$  and the dc-link voltage  $u_{dc}$ . Values  $u_{np\_initial}$  and  $u_{np\_final}$  are the midpoint voltage values at the initial and final instant of the switching period, respectively. As shown in Fig. 6(b),  $u_{np}$  keeps rising in the middle of the switching period, where the positive small vectors are used. After the application of sequences with positive small vectors,  $u_{np\_final}$  is larger than  $u_{np\_initial}$ . On the other hand, according to (9), the change of  $u_{dc}$  is proportional to the integral value of  $(i_{C1} + i_{C2})$ . Therefore, the large current

ripple in  $i_{C1}$  leads to large ripple in  $u_{dc}$  (considering that  $i_{C2}$  has a constant value of  $I_s$ ), as shown in Fig. 6(b). Additionally, the instantaneous dc-link voltage equals the average value  $U_{dc\_ave}$  at the end of the switching period at steady-state operation.

On the other hand, when the midpoint voltage  $u_{np}^{k+1}$  is larger than the desired value, negative small vectors are used. The corresponding switching sequence is applied, as shown in Fig. 7. In inverter I, the dwell times for vectors OOO, ONN, and OON in inverter II are  $0.36T_s$ ,  $0.47T_s$ , and  $0.17T_s$ , respectively. Fig. 8 shows the waveforms of  $i_{C2}$ ,  $u_{np}$ , and  $u_{dc}$ . Considering that now, according to (6),  $i_{C1}$  is equal to  $I_s$  during the whole switching period, the waveform of  $i_{C1}$  is not shown. Similarly, as in Fig. 6, the key values are shown in Fig. 8. As negative small vectors are used, now  $u_{np}$  keeps decreasing and  $u_{np\_final}$  is smaller than  $u_{np\_initial}$ , as shown in Fig. 8(b).

Similarly, another operating point P2 is selected to investigate operation at higher modulation indexes. As shown in Fig. 4(b), the reference vector is located at point P2\_I for inverter I whereas the reference vector is located at point P2\_II for inverter II. In this example, the modulation index is  $m = 0.4$ , and the phase angles of P2\_I and P2\_II are  $7\pi/24$  and  $\pi/8$ , respectively. By using (13), the phase currents are:  $i_a = 0.924I_0$ ,  $i_b = -0.131I_0$ ,  $i_c = -0.793I_0$ ,  $i_d = 0.991I_0$ ,  $i_e = -0.609I_0$ , and  $i_f = -0.382I_0$ , and by using (1), the dc-source current  $I_s$  is equal to  $1.039I_0$ . Figs. 9 and 10 show the waveforms of  $i_{C1}$  and  $i_{C2}$  when the sequence with positive or negative small vectors is utilized, respectively. Note that now neither  $i_{C1}$  nor  $i_{C2}$  is constant, so both waveforms are shown.

As shown in Fig. 9(b),  $i_{C2-sI}$  equals  $0.793I_0$  when vectors PON and PPN are utilized in inverter I while  $i_{C2-sII}$  equals  $0.382I_0$  when vector PON is used in inverter II. Similarly, as shown in Fig. 10(a),  $i_{C1-sI}$  equals  $0.924I_0$  and  $0.793I_0$  when the vectors PON and PPN are used in inverter I, while  $i_{C1-sII}$  equals  $0.991I_0$  when the vector PON is used in inverter II. Therefore, when the middle and large vectors are used, both sequences with positive and negative small vectors generate distinct ripples in  $i_{C1}$  and  $i_{C2}$ . This was not the case for the operating points P1\_I and P1\_II, where the ripple was generated only in the upper/lower capacitor, if the sequence with positive/negative small vectors is used. The overlapping phenomenon still exists, and large current ripples can be observed in waveforms of  $i_{C1}$  and  $i_{C2}$ .

The waveforms of  $u_{np}$  and  $u_{dc}$  at the operating points P2\_I and P2\_II with the sequence with negative or positive small vectors are shown in Fig. 11. Fig. 11(a) shows the midpoint voltage  $u_{np}$  when the sequences with positive small vectors are used in the two inverters. It is observed that the middle vector PON increases  $u_{np}$ . Therefore,  $u_{np}$  keeps increasing during the whole switching period, and  $u_{np\_final}$  is larger than  $u_{np\_initial}$ . The waveform of  $u_{np}$  using the sequence with negative small vectors is presented in Fig. 11(b). The value of  $u_{np}$  decreases when negative small vectors are used but increases when the middle vector PON is used.

Figs. 11(a) and (b) also show the waveforms of  $u_{dc}$ . As mentioned before, the change of  $u_{dc}$  is proportional to the integral value of  $(i_{C1} + i_{C2})$ . The overlapping of  $i_{C1}$  and  $i_{C2}$  leads to a

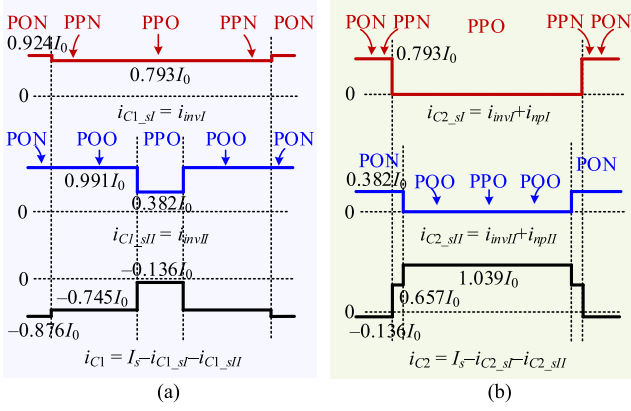


Fig. 9. Current waveforms during a single switching period with the sequence with positive small vectors at operating points P2\_I and P2\_II. (a)  $i_{C1}$  and (b)  $i_{C2}$  and their corresponding components in the two inverters.

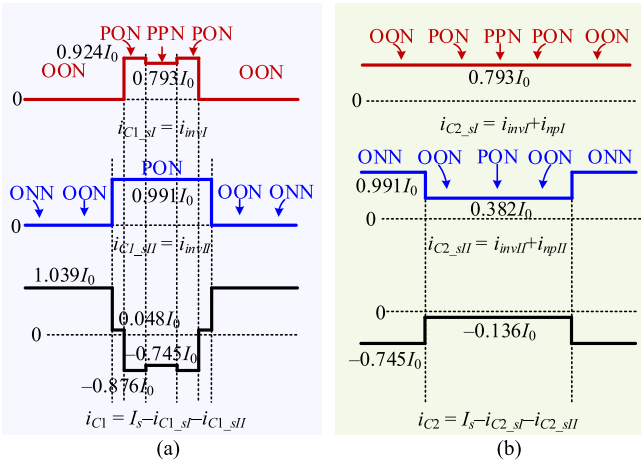


Fig. 10. Current waveforms during a single switching period with the sequence with negative small vectors at operating points P2\_I and P2\_II. (a)  $i_{C1}$  and (b)  $i_{C2}$  and their corresponding components in the two inverters.

longer duration for  $(i_{C1} + i_{C2})$  being positive or negative. As a result, a large voltage ripple occurs in the waveform of  $u_{dc}$ .

#### IV. TSCSS

To mitigate the dc-link current and voltage ripple, a TSCSS is proposed in this article. Fig. 12 shows the principle of the proposed switching strategy. As shown in Fig. 12, the first step is to set two inverters to output switching sequences with small vectors with opposite polarities. There are obviously two ways how this can be done. If the sequence with positive small vectors is used for inverter I and the sequence with negative small vectors for inverter II, which is represented as the first combination 1P2N; or if the sequence with negative small vectors is used for inverter I and the sequence with positive small vectors is used for inverter II, represented as the second combination 1N2P. The choice of combination is determined by their influence on the midpoint voltage. The second step is to rearrange the switching sequence of the two inverters to avoid overlapping of the current peaks and hence reduce the dc-link voltage ripple.

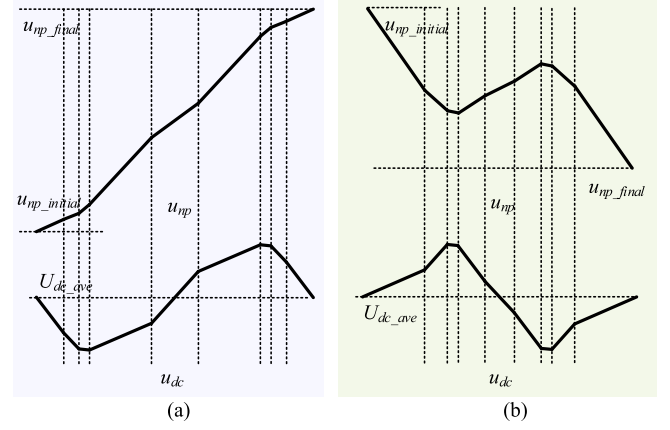


Fig. 11. Midpoint and dc-link voltage waveforms at operating points P2\_I and P2\_II, with a sequence with (a) positive and (b) negative small vectors.

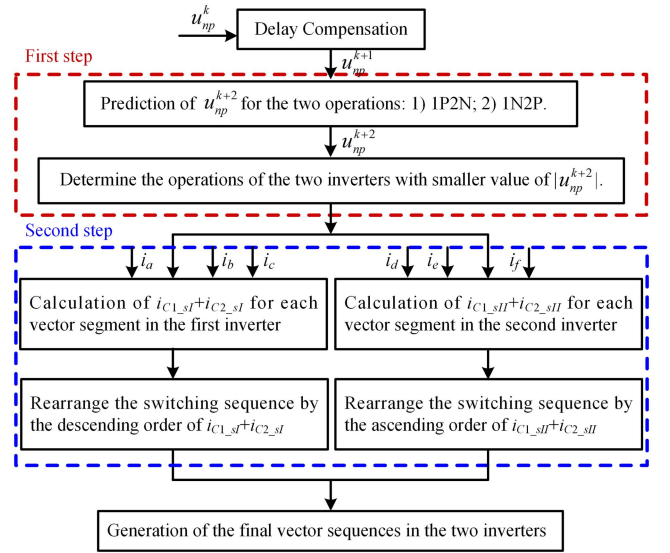


Fig. 12. Principle of the proposed TSCSS.

##### A. First Step: Switching Sequences of Opposite Small Vectors

Based on (5) and (6), the expressions of  $i_{C1\_sI}$  and  $i_{C2\_sI}$  are

$$i_{C1\_sI} = i_{invI} = \sum_x \frac{1}{2} (S_x^2 + S_x) i_x, x \in \{a, b, c\} \quad (14)$$

$$i_{C2\_sI} = i_{invI} + i_{npI} = \sum_x \left( 1 - \frac{1}{2} S_x^2 + \frac{1}{2} S_x \right) i_x, x \in \{a, b, c\}. \quad (15)$$

For negative small vectors,  $S_x$  is  $-1$  or  $0$ , both of which result in  $i_{C1\_sI} = 0$ . On the other hand,  $S_x$  is  $1$  or  $0$  for positive small vectors, and they result in  $i_{C2\_sI} = 0$ . Therefore, the positive small vectors do not generate current ripples in the capacitor  $C_2$ , whereas the negative small vectors do not generate current ripples in the capacitor  $C_1$ . Similar equations to (14) and (15), with the same conclusion, can be written for  $i_{C1\_sII}$  and  $i_{C2\_sII}$ , for  $x \in \{d, e, f\}$ . When two combinations with opposite small vectors are used, the current ripples caused by the two inverters are separated into two capacitors, respectively. Specifically, when

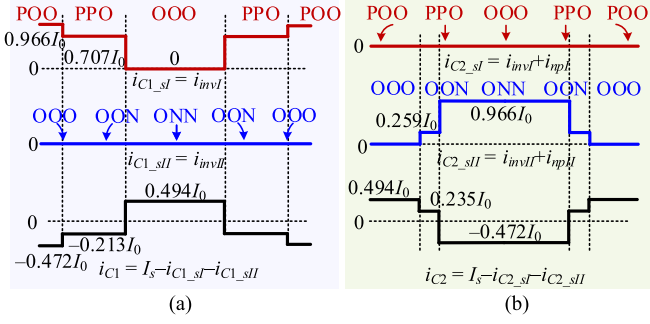


Fig. 13. Current waveforms at operating point P1 with proposed switching strategy using 1P2N mode. (a) Waveforms of  $i_{C1}$ . (b) Waveforms of  $i_{C2}$ .

the switching sequence with positive small vectors is used in inverter I and the switching sequence with negative small vectors is used in inverter II,  $i_{C1-s}$  only contains current peaks from inverter I and  $i_{C2-s}$  only contains current peaks from inverter II. Therefore, current ripples in  $i_{C1}$  and  $i_{C2}$  can be mitigated accordingly.

Further, the midpoint voltage ripple is analyzed. As shown in Figs. 6(b), 8(b), and 11, the utilization of small vectors with the same polarity in the two inverters may cause large midpoint voltage fluctuations. Instead, when the small vectors of opposite polarities are used in the two inverters, the midpoint voltage will not keep increasing or decreasing during a single switching period. Thus, the midpoint voltage fluctuation will be reduced.

As shown in Fig. 12, the choice of 1P2N or 1N2P combination is determined by the balancing effect on the midpoint voltage. Based on (11), the midpoint voltage can be predicted as

$$u_{np}^{k+2} = u_{np}^{k+1} - \frac{1}{2C} \sum_i^{\text{seg}^{k+1}} i_{np-i}^{k+1} t_i^{k+1}. \quad (16)$$

Using (16), the midpoint voltage is predicted for the 1P2N and 1N2P combinations. When  $u_{np}^{k+1}$  is above the desired value, the combination with the lower predicted value of  $u_{np}^{k+2}$  is selected. Contrarily, the combination with the higher predicted value of  $u_{np}^{k+2}$  is selected when  $u_{np}^{k+1}$  is below the desired value.

### B. Second Step: Rearrangement of Switching Sequences

As analyzed above, an effective way to avoid the overlapping between current peaks and reduce ripples is to properly rearrange applied switching sequences in the two inverters. For that purpose, the applied vectors are rearranged in such a way that the considered current in the first inverter is sorted in descending order, whereas in the second inverter, it is sorted in ascending order during the first half of the switching period. It is noted that the ripple of  $u_{dc}$  is proportional to the integral value of  $(i_{C1}+i_{C2})$ , and thus,  $(i_{C1}+i_{C2})$  is used for sorting for reduction of  $u_{dc}$ . Considering that the dc component of  $I_s$  is ignored during evaluation of the voltage and current ripples,  $(i_{C1-s}+i_{C2-s})$  is the current to be considered.

To clearly show the process and advantages of the TSCSS, the operating point P1 using 1P2N mode is selected as an example. Fig. 13 presents the capacitor current waveforms at operating point P1 using 1P2N combination. As shown in Fig. 13(a),

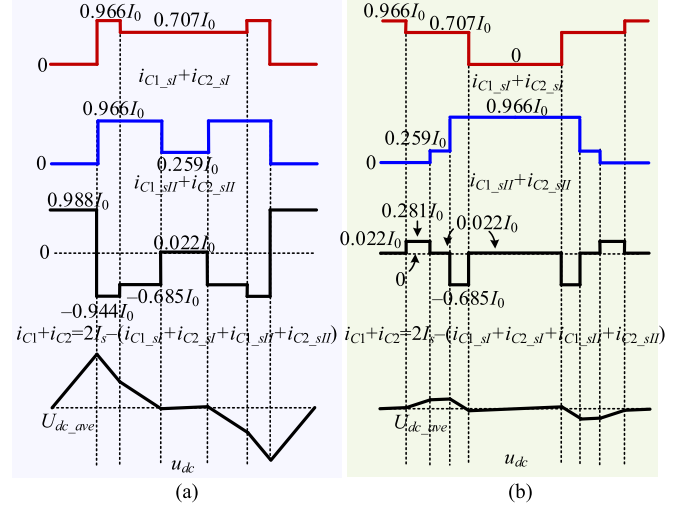


Fig. 14. DC-link voltage waveform comparison at operating point P1 between (a) synchronous method and (b) proposed switching method using 1P2N mode.

$i_{C1-sII}$  is equal to zero because the sequence with negative small vectors is used in inverter II. It can be seen that the switching sequence of inverter I is rearranged now so that  $(i_{C1-sI}+i_{C2-sI})$  is sorted in descending order (during the first half of the switching period). Due to the fact that  $i_{C2-sI}$  equals zero during the whole switching period,  $i_{C1-sI}$  is in descending order, as shown in Fig. 13(a). Compared to the current waveforms in Fig. 6(a), it can be seen that the overlapping between current peaks of the two inverters is avoided and the current ripple is thus reduced. Similar ripple reduction effects can be observed in Fig. 13(b), when compared to the current waveforms in Fig. 8(a). Additionally, the switching sequence of inverter II is rearranged so that  $(i_{C1-sII}+i_{C2-sII})$  is in ascending order. With  $i_{C1-sII}$  equaling zero,  $i_{C2-sII}$  is in ascending order. Hence, by comparison between Figs. 6, 8, and 13, it can be concluded that the TSCSS reduces the dc-link capacitor current ripple.

The dc-link voltage ripple with the synchronous method and with the proposed method is compared in Fig. 14. Since the dc-link voltage is equal to the integral of the sum of the capacitor currents (9), the waveforms of  $(i_{C1}+i_{C2})$  and the corresponding components from the two inverters are also presented in Fig. 14. Fig. 14(a) corresponds to the synchronous switching method of Fig. 6, and Fig. 14(b) shows waveforms using 1P2N mode with the proposed switching method. As shown in Fig. 14(a), the overlapping of current peaks for  $(i_{C1-sI}+i_{C2-sI})$  and  $(i_{C1-sII}+i_{C2-sII})$  directly leads to a large current ripple in  $(i_{C1}+i_{C2})$ . Subsequently, a large voltage ripple is produced in  $u_{dc}$ . On the other hand, the dc-link voltage ripple is significantly reduced with the proposed method in Fig. 14(b), where the switching sequences of two inverters are rearranged such that  $(i_{C1-sI}+i_{C2-sI})$  is in descending order and  $(i_{C1-sII}+i_{C2-sII})$  is in ascending order. Therefore, the overlapping of current peaks in  $(i_{C1-sI}+i_{C2-sI})$  and  $(i_{C1-sII}+i_{C2-sII})$  is avoided.

Fig. 15 compares the midpoint voltage ripple with the synchronous method and the proposed switching method, where the waveforms of  $i_{npI}$ ,  $i_{npII}$ , and  $i_{np}$  are presented. It can be seen in Fig. 15(a) that both  $i_{npI}$  and  $i_{npII}$  are below or equal to

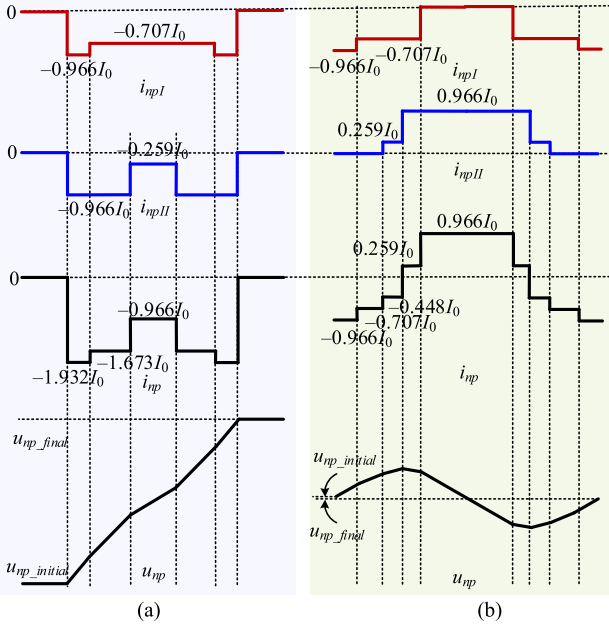


Fig. 15. Midpoint voltage comparison at operating point P1 between (a) synchronous method and (b) proposed switching method using 1P2N mode.

TABLE I  
COMPARISON OF CURRENT RIPPLES BETWEEN SYNCHRONOUS METHOD AND PROPOSED TWO-STEP METHOD

Operating point	Method type	$i_{C1}$	$i_{C2}$
P1	Synchronous method	1.932 $I_0$	1.932 $I_0$
	Proposed method	0.966 $I_0$	0.966 $I_0$
P2	Synchronous method	1.915 $I_0$	1.784 $I_0$
	Proposed method	1.122 $I_0$	1.402 $I_0$

zero. Therefore,  $i_{np}$  is also below or equal to zero during the whole switching period. Consequently, a large deviation of the midpoint voltage appears in Fig. 15(a). On the other hand,  $i_{npI}$  is below or equal to zero, whereas  $i_{npII}$  is above or equal to zero, with the proposed switching method in Fig. 15(b). Hence, the polarity distribution of  $i_{np}$  is more balanced within the switching period. As a result, the deviation of  $u_{np}$  in Fig. 15(b) is much smaller than in Fig. 15(a), and the midpoint voltage ripple is reduced with the proposed method.

Using similar analysis as in Figs. 13–15, operating point P1 for 1N2P mode can be also analyzed. As a final result, it can be obtained that  $i_{C1}$  waveform would look like  $i_{C2}$  waveform from Fig. 13(b);  $i_{C2}$  would look like  $i_{C1}$  from Fig. 13(a);  $u_{np}$  would be a mirrored image of  $u_{np}$  from Fig. 15(b) (multiplied by  $-1$ ); and  $u_{dc}$  would be of the same shape as  $u_{dc}$  in Fig. 14(b). Of course, in 1N2P mode, different space vectors would be applied. Finally, for completeness, the final current and voltage waveforms for the operating point P2 (with the proposed method) are shown in Fig. 16. Similar ripple mitigation effects can be observed when compared to the adequate waveforms ( $i_{C1}$ ,  $i_{C2}$ ,  $u_{np}$ ,  $u_{dc}$ ) in Figs. 9–11 where the synchronous method was used. In summary, the amplitudes of peak-to-peak current ripples are compared in Table I. It can be observed that the peak-to-peak current ripple is significantly reduced with the proposed collaborative switching strategy.

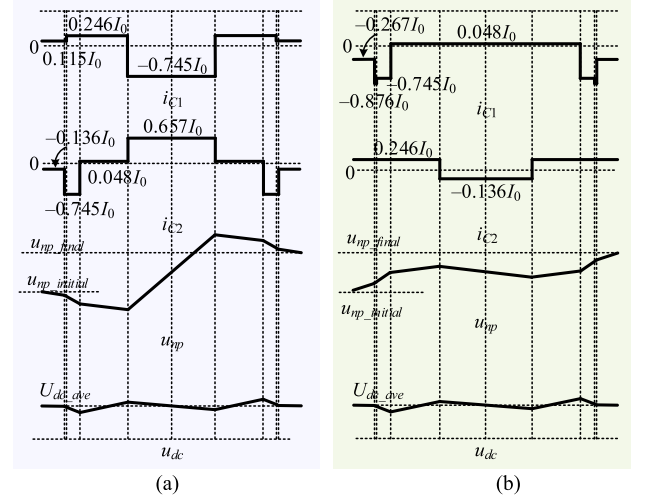


Fig. 16. Current and voltage waveforms at operating points P2\_I and P2\_II with the proposed switching strategy: (a) 1P2N and (b) 1N2P operation.

## V. PERFORMANCE ANALYSIS

### A. Influence of Vectors on Midpoint Voltage Balancing

As shown in (11), the reason for fluctuation in the midpoint voltage is the utilization of vectors containing O levels (small and middle vectors), which generate  $i_{np}$ . To verify the voltage balancing capability of the proposed strategy, the effects of small vectors and middle vectors are separated. Inverter I is selected for analysis, and the same applies to inverter II.

First, the effects of the middle vectors on the midpoint voltage are analyzed. The term  $d(m, \theta)$  represents the duty cycle of the middle vector in sectors S1–S6, which is determined by the modulation index  $m$  and the phase angle  $\theta$  of the reference vector. In S1, the middle vector is PON, and  $i_{np} = i_b$ . The increment of the midpoint voltage influenced by PON during the whole sector S1, namely  $\Delta u_{np\_S1}$ , is

$$\Delta u_{np\_S1} = -\frac{1}{2\omega C} \int_0^{\pi/3} i_b(\theta) d(m, \theta) d\theta. \quad (17)$$

Similarly, the increment on midpoint voltage during the whole sector S2 (as a consequence of OPN), namely  $\Delta u_{np\_S2}$ , can be calculated as

$$\begin{aligned} \Delta u_{np\_S2} &= -\frac{1}{2\omega C} \int_{\pi/3}^{2\pi/3} i_a(\theta) d(m, \theta) d\theta \\ &= -\frac{1}{2\omega C} \int_0^{\pi/3} i_a\left(\theta + \frac{\pi}{3}\right) d\left(m, \theta + \frac{\pi}{3}\right) d\theta \end{aligned} \quad (18)$$

where  $d(m, \theta) = d(m, \theta + \pi/3)$  because of symmetry. Also, for a symmetrical three-phase system  $i_b(\theta) = -i_a(\theta + \pi/3)$ . Therefore, the total increment of the midpoint voltage caused by the middle vectors equals zero from the beginning of sector S1 to the end of sector S2, as

$$u_{np}|_{\omega t=2\pi/3} - u_{np}|_{\omega t=0} = \Delta u_{np\_S1} + \Delta u_{np\_S2} = 0. \quad (19)$$

The same applies to sectors S3–S4 and S5–S6. Consequently, it can be concluded that the middle vectors do not generate

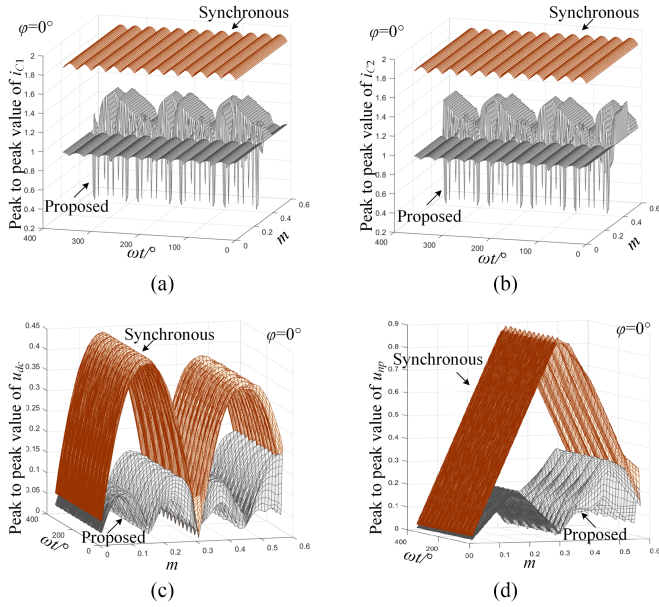


Fig. 17. Ripple amplitude comparison of  $i_{C1}$ ,  $i_{C2}$ ,  $u_{dc}$ , and  $u_{np}$  with unity power factor. (a)  $i_{C1}$ . (b)  $i_{C2}$ . (c)  $u_{dc}$ . (d)  $u_{np}$ .

midpoint voltage dc deviation. Instead, fluctuation of the third harmonic frequency can be observed in the midpoint voltage, which is an inherent problem of SVPWM in NPC-3L inverters [33]. At low power factor operations, whether to enable the first step optimization (opposite small vector sequences) can be determined by the difference between the sampled and desired midpoint voltage value. In practice, this problem can be mitigated by appropriate sizing of the dc-link capacitors.

Second, the effect of the small vectors on the mid-point voltage is analyzed. Midpoint current  $i_{np}$  generated by the sequence with positive small vectors is opposite to the one generated by the sequence with negative small vectors. For example,  $i_{np}$  generated by the positive small vector POO is  $i_b + i_c = -i_a$ , whereas  $i_{np}$  generated by the negative small vector ONN is  $i_a$ . Furthermore,  $i_{np}$  generated in operation 1P2N is opposite to that in operation 1N2P. Accordingly, the integral values of  $i_{np}$  in 1P2N and 1N2P combination are opposite to each other. Consequently, the opposite small vector sequences operation can ensure the balance of the dc-link capacitor voltages.

### B. Ripple Reduction Under Different Operations

To comprehensively show the effect of the ripple reduction by the proposed switching strategy, Figs. 17–19 compare the amplitudes of ripples in  $i_{C1}$ ,  $i_{C2}$ ,  $u_{dc}$ , and  $u_{np}$  with three different power factor angles, namely  $0^\circ$ ,  $-30^\circ$ , and  $30^\circ$ , respectively. Specifically, the small vector sequences of the same polarity are used in the two inverters with the SSS (used polarity depends on deviation of the midpoint voltage). For the proposed switching strategy, 1P2N or 1N2P operation is used (as per the first step of the algorithm in Fig. 12). The current and voltage values are given in per unit values in Figs. 17–19. The current base is  $I_0$  and the voltage base is  $I_0 T_s / C$ .

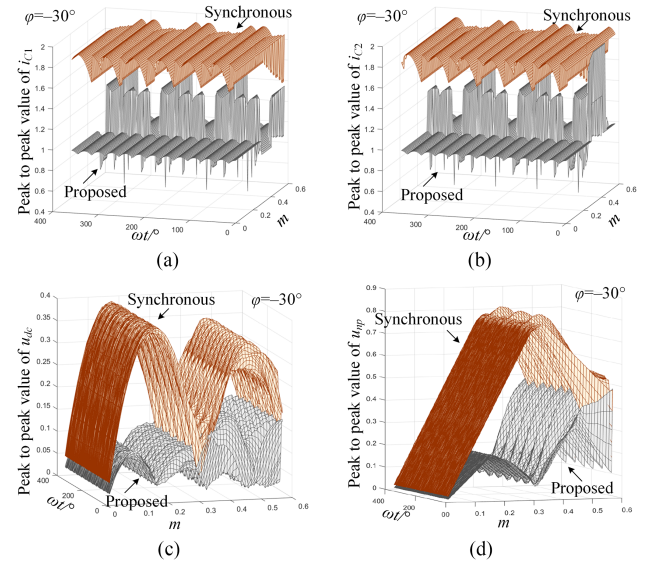


Fig. 18. Ripple amplitude comparison of  $i_{C1}$ ,  $i_{C2}$ ,  $u_{dc}$ , and  $u_{np}$  with  $\varphi = -30^\circ$ . (a)  $i_{C1}$ . (b)  $i_{C2}$ . (c)  $u_{dc}$ . (d)  $u_{np}$ .

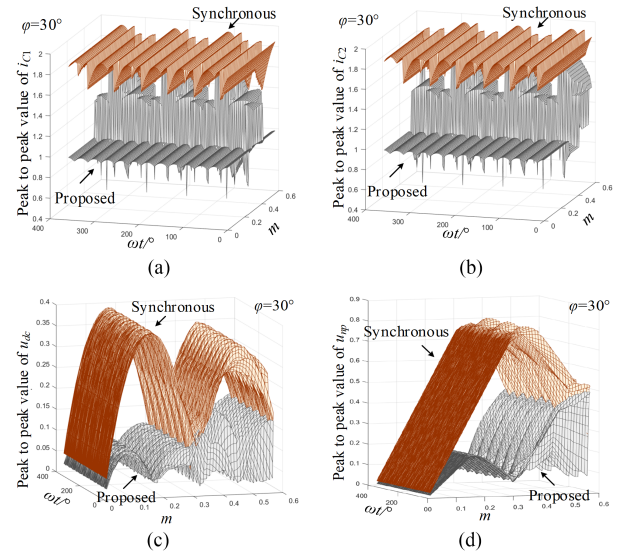


Fig. 19. Ripple amplitude comparison of  $i_{C1}$ ,  $i_{C2}$ ,  $u_{dc}$ , and  $u_{np}$  with  $\varphi = 30^\circ$ . (a)  $i_{C1}$ . (b)  $i_{C2}$ . (c)  $u_{dc}$ . (d)  $u_{np}$ .

Fig. 17(a) shows numerical comparison results of  $i_{C1}$  ripple amplitude with unity power factor. It can be observed that the ripple of  $i_{C1}$  using the proposed switching strategy is lower than that using the SSS (for any value of  $\omega t$  and  $m$ ). Similar results are obtained for  $i_{C2}$ , and are shown in Fig. 17(b). Fig. 17(c) shows the comparison results for  $u_{dc}$ . The ripple of  $u_{dc}$  using the proposed switching strategy is lower than that using the SSS. Fig. 17(d) shows the comparison result for  $u_{np}$ . The ripple reduction of  $u_{np}$  is significant under low modulation index operation while it is less effective under high modulation index operation. The reason is in the utilization of middle vectors. Both comparisons under phase-leading and phase-lagging power factor angles in Figs. 18 and 19 show similar results to those in Fig. 17 at unity power factor. Therefore, it indicates that current

TABLE II  
 KEY PARAMETERS OF EXPERIMENTAL SETUP

Name	Value
Pole pair number	3
$q$ -axis inductance	6.21 mH
$d$ -axis inductance	6.21 mH
PM flux (amplitude)	0.20 Wb
Stator resistance	0.21 $\Omega$
DC-link capacitance	1000 $\mu$ F
Sampling frequency	2 kHz
DC-link voltage	100 V

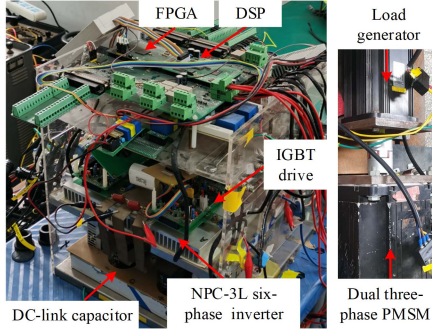


Fig. 20. Photograph of the experimental setup.

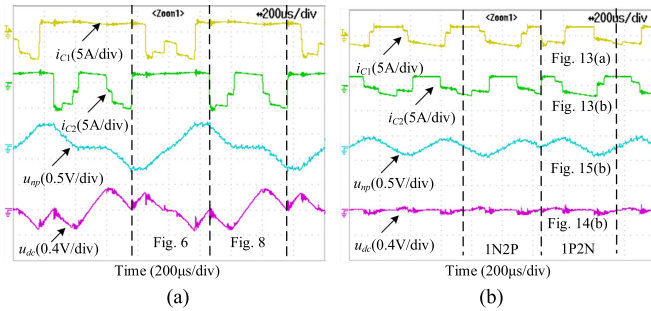


Fig. 21. Current and voltage waveforms at operating point P1 with (a) synchronous method and (b) proposed switching method.

and voltage ripples in the dc link can be reduced under different power factors with the proposed collaborative switching strategy.

## VI. EXPERIMENTAL VERIFICATION

The experiments are carried out on a laboratory prototype of NPC-3L inverter-fed dual three-phase PMSM drive to validate the proposed switching strategy. The key system parameters are shown in Table II. A photograph of the experimental setup is shown in Fig. 20. The control algorithm is implemented on DSP (TMS320F28346), while the PWM inverter gating signals are generated by FPGA (Xilinx-Spartan6 XC6SLX25). A three-phase synchronous generator, mechanically coupled to the dual three-phase PMSM, is used as a load.

First, the experimental current and voltage waveforms in Figs. 21 and 22, at typical operating points P1 and P2, and with different switching methods, are compared with the theoretical analysis (Figs. 6, 8–11, 13–16). Fig. 21 shows the measurement

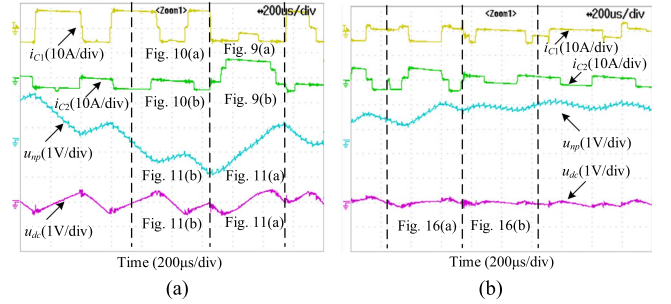


Fig. 22. Current and voltage waveforms at operating point P2 with (a) synchronous method and (b) proposed switching method.

results at P1. The synchronous switching method is used in Fig. 21(a) whereas the proposed TSCSS is used in Fig. 21(b). Fig. 21(a) agrees well with the analysis in Figs. 6 and 8, while Fig. 21(b) corresponds to the analysis in Figs. 13–15. Note that the algorithm is dynamically choosing if the positive or negative vectors (i.e., 1N2P or 1P2N for the proposed method) are used in each switching period. Thus, the switching periods to be compared with the relevant theoretical analysis are clearly denoted in Figs. 21 and 22. Fig. 22 presents measurement results at operating point P2. The synchronous switching method is used in Fig. 22(a) whereas the proposed method is used in Fig. 22(b). Specifically, Fig. 22(a) corresponds to the analysis in Figs. 9–11. Fig. 22(b) corresponds to the analysis in Fig. 16. It should be noted that the actual duty cycle of each switching sequence is slightly different from theoretical analysis since the waveforms are measured within two consecutive switching periods. From previous comparison, it can be concluded that the experimental results at both operating points well agree with the theoretical analysis. The concerned ripples are effectively mitigated after applying the proposed switching method.

Second, the steady-state waveforms of current and voltage ripples are compared for different switching strategies in Figs. 23 and 24 ( $n$  represents machine speed). Applied strategies are denoted as: SSS stands for synchronous switching strategy, FSCSS represents the switching strategy with opposite small vector sequences in the first step of the algorithm only, SSCSS represents the switching strategy with rearranged switching sequences in the second step of the algorithm only, and TSCSS represents the proposed two-step collaborative switching strategy. FSCSS and SSCSS are established from the proposed TSCSS to verify the necessity of both the two steps in the proposed algorithm. Operation at two different modulation indexes is achieved by changing the speed of the machine. Specifically, the modulation index equals 0.24 and 0.50 at speeds of 300 and 600 r/min, respectively. The fundamental stator frequencies are 15 and 30 Hz at the speed of 300 and 600 r/min, respectively, and the corresponding power factor angles are  $-16^\circ$  and  $-27^\circ$ , respectively. All the capacitor current and voltage ripple waveforms are measured by the ac coupling of probes. Fig. 23(a) and (b) show the comparison results of the dc-link voltage ripple. As shown in Fig. 23, SSCSS and TSCSS possess lower dc-link voltage ripple compared to SSS and FSCSS at both modulation index values. Therefore, it verifies that the rearrangement of the switching sequence in the

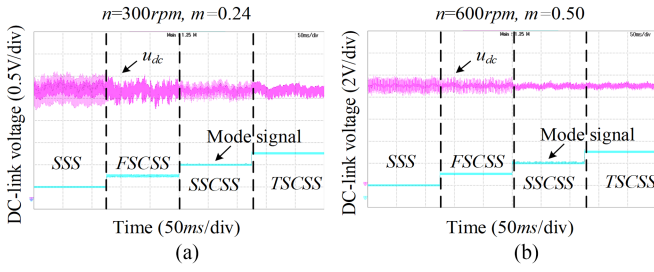


Fig. 23. Comparison of the DC-link voltage ripples with different switching strategies. (a)  $m = 0.24$ . (b)  $m = 0.50$ .

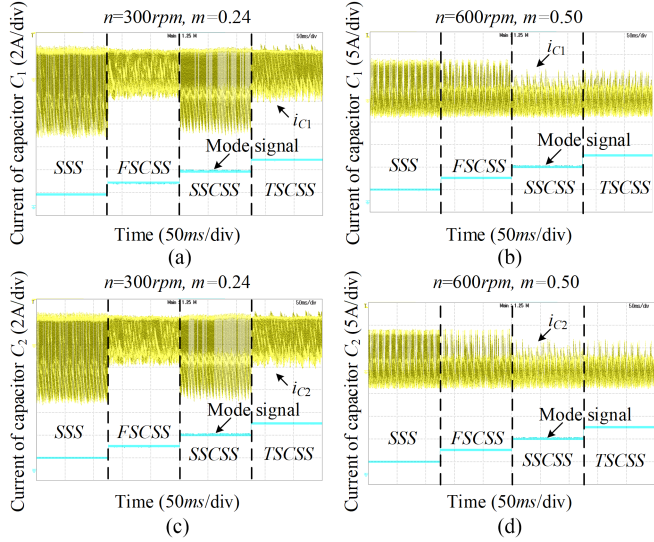


Fig. 24. Comparison of steady-state current ripples of the capacitors. Current ripple of  $C_1$  at (a)  $m = 0.24$ , (b)  $m = 0.50$ , and of  $C_2$  at (c)  $m = 0.24$  and (d)  $m = 0.50$ .

second step of the proposed algorithm can effectively mitigate the dc-link voltage ripple.

Fig. 24 presents the comparison results of the capacitor current ripples using different switching strategies. As shown in Fig. 24(a), the current ripple in  $C_1$  with FSCSS and TSCSS is lower than that with SSS and SSCSS. The reason is that, as analyzed in Section IV-A,  $i_{C1}$  equals  $I_s$  when sequences with negative small vectors are used. Therefore, SSCSS can only reduce the peak-to-peak current ripple in  $C_1$  during the intervals when using sequences with positive small vectors. However, sequences with positive and negative small vectors are used alternately in the two inverters in practical operation. Fig. 24(b) shows the comparison results at a modulation index of 0.50. It is observed that both the proposed TSCSS and the SSCSS have lower current ripple amplitude than SSS and FSCSS. The reason lies in the fact that both middle and large vectors will generate current ripples in the two capacitors, respectively. Therefore, under high modulation index operation, only the opposite small vector operation in the first step cannot ensure that the current ripples caused by the two inverters are separated into two capacitors, respectively. Consequently, with the rearranged sequences in the second step, the ripples in the two capacitors can be mitigated more effectively. Fig. 24(c) and (d) are the current

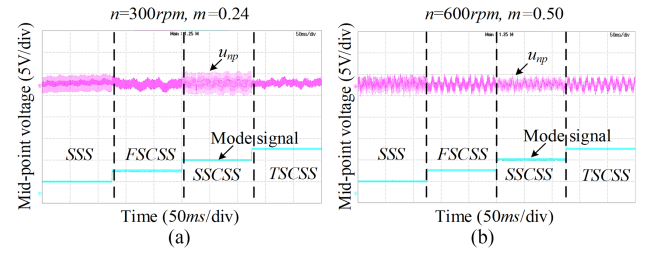


Fig. 25. Comparison of steady-state midpoint voltage waveforms with different switching strategies. (a)  $m = 0.24$ . (b)  $m = 0.50$ .

waveforms of capacitor  $C_2$  under low and high modulation index operation, respectively. The results and conclusions are similar to those in capacitor  $C_1$  [Fig. 24(a) and (b)].

Fig. 25 compares the control performance of the midpoint voltage using four different switching strategies. As shown in Fig. 25(a), the fluctuation range of the midpoint voltage with SSCSS is similar to that with SSS. The reason lies in the fact that the rearrangement of the switching sequence cannot influence the integral value of the neutral point current during the whole switching period. On the other hand, FSCSS and TSCSS can provide much smaller ripples in the midpoint voltage waveform by using the opposite small vector sequences in two inverters. As shown in Fig. 25(b), the midpoint voltage ripple amplitude is almost the same for all switching strategies under high modulation index operation. Furthermore, it can be observed that only the third-order harmonic ripple exists when FSCSS and TSCSS are utilized. It verifies that the ripples generated by the small vectors can be reduced effectively with the proposed TSCSS while the third-order harmonic ripple caused by the middle vectors cannot be mitigated under high modulation index conditions. According to the steady-state experimental results shown in Figs. 23–25, it can be concluded that the proposed TSCSS possesses the best ripple mitigation capability among the four switching strategies at both low and high modulation index operation.

To verify the influence of the power factor on ripple reduction, the power factor angle was changed by adjusting the  $d$ -axis current of the machine. However, the same conclusions were reached. For low modulation indexes, all ripples are reduced, regardless of the power factor angle. Yet, for high modulation index values, capacitor current and the dc-link voltage ripples are reduced, while the high-frequency fluctuation in the midpoint voltage is mitigated with the proposed switching method.

Finally, the current ripple and the midpoint voltage fluctuation waveforms of SSS and the proposed TSCSS are compared during dynamic response. The speed reference value  $n_{ref}$  is step changed from 300 to 600 r/min. Fig. 26 presents the current ripple waveforms in capacitors  $C_1$  and  $C_2$ , respectively. The same conclusions as for the steady state results in Fig. 24 can be drawn. During the dynamic response, the current ripples in the capacitors  $C_1$  and  $C_2$  using the proposed TSCSS are always smaller than those using SSS. Fig. 27 shows the comparison of the midpoint voltage during dynamic operation. Clearly, conclusions related to the ripple reduction are consistent with the steady-state results shown in Fig. 25. Besides, the total harmonic distortion (THD) values of stator current in phase

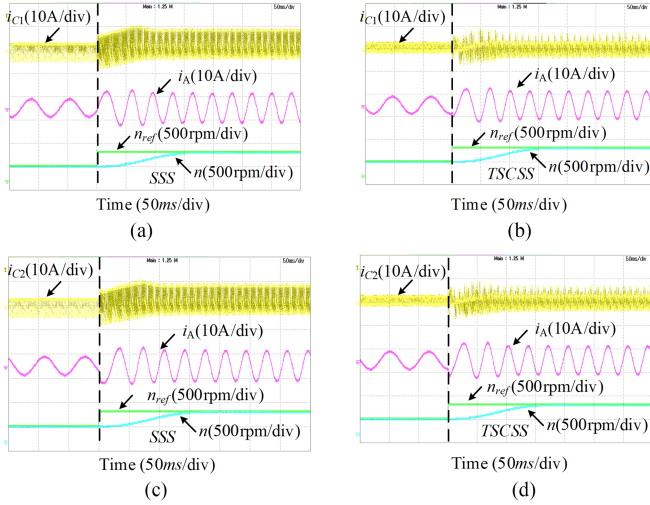


Fig. 26. Capacitor current ripples with different switching strategies during the transient. Current ripple of  $C_1$  (a) with SSS and (b) proposed TSCSS, and current ripple of  $C_2$  (c) with SSS and (d) with proposed TSCSS.

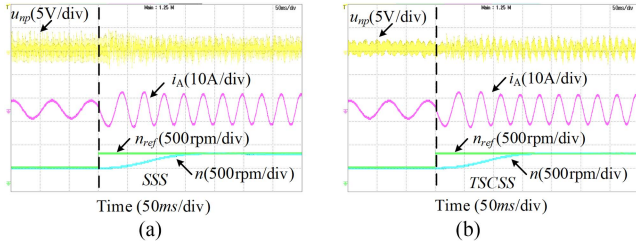


Fig. 27. Midpoint voltage waveforms with different switching strategies during the transient. (a) SSS. (b) Proposed TSCSS.

A at a modulation index of 0.24 using SSS and TSCSS are found to be 5.45% and 6.03%, respectively. The THD values at a modulation index of 0.50 using SSS and TSCSS are 4.42% and 4.86%, respectively. The proposed TSCSS generates slightly higher but acceptable THD values in stator currents, which is due to the rearrangement of the switching sequences.

## VII. CONCLUSION

In this article, a TSCSS has been proposed to mitigate the current and voltage dc-link ripples in an NPC-3L inverter-fed dual three-phase PMSM drive. The first step is to select switching sequences including opposite small vectors for the two inverters, and the second step is to rearrange switching states of the two inverters in order of the sum of their current components in the upper and lower capacitors in the dc link. The proposed collaborative switching strategy possesses the following advantages: lower current ripples in the dc-link capacitors and smaller dc-link voltage ripples, which are achieved under both low and high modulation index operation. The peak-to-peak fluctuation of the midpoint voltage can be reduced under low modulation index operation, while the high-frequency voltage fluctuation can be mitigated under high modulation index operation. The experimental results have been presented to verify the validity of the proposed collaborative switching strategy. Reduced dc-link

voltage and current ripples can not only reduce the dc-link capacitance but could also facilitate extension of the lifetime and reliability of the dc-link capacitors.

## REFERENCES

- [1] E. Levi, "Multiphase electric machines for variable-speed applications," *IEEE Trans. Ind. Electron.*, vol. 55, no. 5, pp. 1893–1909, May 2008.
- [2] F. Barrero and M. J. Duran, "Recent advances in the design, modeling, and control of multiphase machines—Part I," *IEEE Trans. Ind. Electron.*, vol. 63, no. 1, pp. 449–458, Jan. 2016.
- [3] M. Mengoni, L. Zarri, A. Tani, L. Parsa, G. Serra, and D. Casadei, "High-torque-density control of multiphase induction motor drives operating over a wide speed range," *IEEE Trans. Ind. Electron.*, vol. 62, no. 2, pp. 814–825, Feb. 2015.
- [4] Z. Wang, X. Wang, J. Cao, M. Cheng, and Y. Hu, "Direct torque control of T-NPC inverters-fed double-stator-winding PMSM drives with SVM," *IEEE Trans. Power Electron.*, vol. 33, no. 2, pp. 1541–1553, Feb. 2018.
- [5] O. Dordevic, E. Levi, and M. Jones, "A vector space decomposition based space vector PWM algorithm for a three-level seven-phase voltage source inverter," *IEEE Trans. Power Electron.*, vol. 28, no. 2, pp. 637–649, Feb. 2013.
- [6] J. Rodriguez, S. Bernet, B. Wu, J. O. Pontt, and S. Kouro, "Multi-level voltage-source-converter topologies for industrial medium-voltage drives," *IEEE Trans. Ind. Electron.*, vol. 54, no. 6, pp. 2930–2945, Dec. 2007.
- [7] Z. Wang, Y. Wang, J. Chen, and Y. Hu, "Decoupled vector space decomposition based space vector modulation for dual three-phase three-level motor drives," *IEEE Trans. Power Electron.*, vol. 33, no. 12, pp. 10683–10697, Dec. 2018.
- [8] M. Gu, Z. Wang, K. Yu, X. Wang, and M. Cheng, "Interleaved model predictive control for three-level neutral-point-clamped dual three-phase PMSM drives with low switching frequencies," *IEEE Trans. Power Electron.*, vol. 36, no. 10, pp. 11618–11630, Oct. 2021.
- [9] E. Levi, "Advances in converter control and innovative exploitation of additional degrees of freedom for multiphase machines," *IEEE Trans. Ind. Electron.*, vol. 63, no. 1, pp. 433–448, Jan. 2016.
- [10] X. Wang, Z. Wang, Z. Xu, M. Cheng, W. Wang, and Y. Hu, "Comprehensive diagnosis and tolerance strategies for electrical faults and sensor faults in dual three-phase PMSM drives," *IEEE Trans. Power Electron.*, vol. 34, no. 7, pp. 6669–6684, Jul. 2019.
- [11] S. Yang, D. Xiang, A. Bryant, P. Mawby, L. Ran, and P. Tavner, "Condition monitoring for device reliability in power electronic converters: A review," *IEEE Trans. Power Electron.*, vol. 25, no. 11, pp. 2734–2752, Nov. 2010.
- [12] M. L. Gasperi, "Life prediction modeling of bus capacitors in AC variable-frequency drives," *IEEE Trans. Ind. Appl.*, vol. 41, no. 6, pp. 1430–1435, Nov./Dec. 2005.
- [13] M. A. Vogelsberger, T. Wiesinger, and H. Ertl, "Life-cycle monitoring and voltage-managing unit for DC-link electrolytic capacitors in PWM converters," *IEEE Trans. Power Electron.*, vol. 26, no. 2, pp. 493–503, Feb. 2011.
- [14] P. Alemi, Y. Jeung, and D. Lee, "DC-link capacitance minimization in T-type three-level AC/DC/AC PWM converters," *IEEE Trans. Ind. Electron.*, vol. 62, no. 3, pp. 1382–1391, Mar. 2015.
- [15] I. Won, K. Lee, and Y. Cho, "An optimized switching scheme for DC-link current ripple reduction in three-level T-type inverter," in *Proc. IEEE Appl. Power Electron. Conf. Expo.*, 2017, pp. 3415–3419.
- [16] S. Kim, I. J. Won, J. Kim, and K. Lee, "DC-link ripple current reduction method for three-level inverters with optimal switching pattern," *IEEE Trans. Ind. Electron.*, vol. 65, no. 12, pp. 9204–9214, Dec. 2018.
- [17] Y. J. Kim, S. M. Kim, and K. B. Lee, "Improving DC-link capacitor lifetime for three-level photovoltaic hybrid active NPC inverters in full modulation index range," *IEEE Trans. Power Electron.*, vol. 36, no. 5, pp. 5250–5261, May 2021.
- [18] L. Kai, L. Mengshu, L. Zhengfeng, D. Zhenghua, and T. Shaoju, "Analytical closed-form expressions of DC current ripple for three-level neutral point clamped inverters with space-vector pulse-width modulation," *IET Power Electron.*, vol. 9, no. 5, pp. 930–937, Apr. 2016.
- [19] K. Choi, S. Kim, S. Jung, and R. Kim, "Generalized switching modification method using carrier shift for DC-link capacitor RMS current reduction in real-time implementation," *IEEE Trans. Ind. Electron.*, vol. 66, no. 8, pp. 5992–6001, Aug. 2019.

- [20] Z. Wang, X. Wang, X. Yang, C. Wen, Y. Gong, and Y. Hu, "Mitigation of DC-link current ripple for dual three-phase flux-adjustable hybrid PMAC drives using collaborative switching strategy," *IEEE Trans. Ind. Electron.*, vol. 67, no. 9, pp. 7202–7216, Sep. 2020.
- [21] X. Pei, W. Zhou, and Y. Kang, "Analysis and calculation of DC-link current and voltage ripples for three-phase inverter with unbalanced load," *IEEE Trans. Power Electron.*, vol. 30, no. 10, pp. 5401–5412, Oct. 2015.
- [22] T. Chen, S. Li, and B. Fahimi, "Analysis of DC-link voltage ripple in voltage source inverters without electrolytic capacitor," in *Proc. 44th Annu. Conf. IEEE Ind. Electron. Soc.*, 2018, pp. 1041–1048.
- [23] C. Rettner, G. Jacob, M. Schiedermeier, A. Apelsmeier, and M. März, "Voltage ripple analysis based on DC-link current harmonics for voltage source inverters," in *Proc. 20th Workshop Control Model. Power Electron.*, 2019, pp. 1–6.
- [24] M. Vujacic, O. Dordevic, and G. Grandi, "Evaluation of DC-link voltage ripple in seven-phase PWM voltage source inverters," in *Proc. IEEE Int. Telecommun. Energy Conf.*, 2018, pp. 1–6.
- [25] M. Vujacic, O. Dordevic, and G. Grandi, "Evaluation of DC-link voltage switching ripple in multiphase PWM voltage source inverters," *IEEE Trans. Power Electron.*, vol. 35, no. 4, pp. 3478–3490, Apr. 2020.
- [26] S. Bhattacharya, D. Mascarella, G. Joos, J. M. Cyr, and J. Xu, "A dual three-level T-NPC inverter for high-power traction applications," *IEEE J. Emer. Sel. Topics Power Electron.*, vol. 4, no. 2, pp. 668–678, Jun. 2016.
- [27] M. Schweizer, T. Friedli, and J. W. Kolar, "Comparative evaluation of advanced three-phase three-level inverter/converter topologies against two-level systems," *IEEE Trans. Ind. Electron.*, vol. 60, no. 12, pp. 5515–5527, Dec. 2013.
- [28] M. Schweizer and J. W. Kolar, "Design and implementation of a highly efficient three-level T-type converter for low-voltage applications," *IEEE Trans. Power Electron.*, vol. 28, no. 2, pp. 899–907, Feb. 2013.
- [29] X. Wang, Z. Wang, M. Gu, D. Xiao, J. He, and A. Emadi, "Diagnosis-free self-healing scheme for open-circuit faults in dual three-phase PMSM drives," *IEEE Trans. Power Electron.*, vol. 35, no. 11, pp. 12053–12071, Nov. 2020.
- [30] X. Wang, Z. Wang, Z. Xu, J. He, and W. Zhao, "Diagnosis and tolerance of common electrical faults in T-type three-level inverters fed dual three-phase PMSM drives," *IEEE Trans. Power Electron.*, vol. 35, no. 2, pp. 1753–1769, Feb. 2020.
- [31] X. Wang, Z. Wang, M. Cheng, and Y. Hu, "Remedial strategies of T-NPC three-level asymmetric six-phase PMSM drives based on SVM-DTC," *IEEE Trans. Ind. Electron.*, vol. 64, no. 9, pp. 6841–6853, Sep. 2017.
- [32] L. Dalessandro, S. D. Round, U. Drogenik, and J. W. Kolar, "Discontinuous space-vector modulation for three-level PWM rectifiers," *IEEE Trans. Power Electron.*, vol. 23, no. 2, pp. 530–542, Mar. 2008.
- [33] K. Chen, W. Jiang, and P. Wang, "An extended DPWM strategy with unconditional balanced neutral point voltage for neutral point clamped three-level converter," *IEEE Trans. Ind. Electron.*, vol. 66, no. 11, pp. 8402–8413, Nov. 2019.



**Minrui Gu** (Student Member, IEEE) received the B.S. degree from the Nanjing University of Science and Technology, Nanjing, China, in 2019, and the M.S. degree in 2021 from Southeast University, Nanjing, where he is currently working toward the Ph.D. degree, all in electrical engineering.

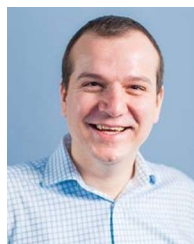
His research interests include control of multiphase permanent magnet synchronous motors and modulation of multilevel converters.



**Zheng Wang** (Senior Member, IEEE) received the B.Eng. and M.Eng. degrees from Southeast University, Nanjing, China, in 2000 and 2003, respectively, and the Ph.D. degree from The University of Hong Kong, Hong Kong, in 2008.

From 2008 to 2009, he was a Postdoctoral Fellow with Ryerson University, Toronto, ON, Canada. He is currently a Full Professor with the School of Electrical Engineering, Southeast University. He has authored more than 100 internationally refereed papers, one English book published by IEEE-Wiley Press, and two English book chapters in the areas of his research interests, which include electric drives, power electronics, and renewable power generation.

Prof. Wang was the recipient of the IEEE PES Chapter Outstanding Engineer Award, the Outstanding Young Scholar Award of Jiangsu Natural Science Foundation of China, and several paper awards of journals and conferences. He is an Associate Editor for IEEE TRANSACTIONS ON INDUSTRIAL ELECTRONICS and *Journal of Power Electronics*.



**Obrad Dordevic** (Member, IEEE) received the Dipl. Ing. degree in electronic engineering from the University of Belgrade, Belgrade, Serbia, in 2008.

In 2009, he was a Ph.D. Student with Liverpool John Moores University, Liverpool, U.K., where he was appointed as a Lecturer, in May 2013. In 2018, he was promoted to a Reader in Power Electronics. His main research interests include power electronics, electrostatic precipitators, and advanced variable-speed multiphase drive systems.